



HAL
open science

Influence of Cluster Sources on the Growth Mechanisms and Chemical Composition of Bimetallic Nanoparticles

Murilo Moreira, Levi C Felix, Emmanuel Cottancin, Michel Pellarin, Daniel Ugarte, Matthias Hillenkamp, Douglas S Galvao, Varlei Rodrigues

► **To cite this version:**

Murilo Moreira, Levi C Felix, Emmanuel Cottancin, Michel Pellarin, Daniel Ugarte, et al.. Influence of Cluster Sources on the Growth Mechanisms and Chemical Composition of Bimetallic Nanoparticles. *Journal of Physical Chemistry C*, 2023, 127 (4), pp.1944-1954. 10.1021/acs.jpcc.2c08044 . hal-04215250

HAL Id: hal-04215250

<https://hal.science/hal-04215250>

Submitted on 22 Sep 2023

HAL is a multi-disciplinary open access archive for the deposit and dissemination of scientific research documents, whether they are published or not. The documents may come from teaching and research institutions in France or abroad, or from public or private research centers.

L'archive ouverte pluridisciplinaire **HAL**, est destinée au dépôt et à la diffusion de documents scientifiques de niveau recherche, publiés ou non, émanant des établissements d'enseignement et de recherche français ou étrangers, des laboratoires publics ou privés.

Influence of Cluster Sources on the Growth Mechanisms and Chemical Composition of Bimetallic Nanoparticles

Murilo Moreira,^{†,‡,¶} Levi C. Felix,^{†,¶} Emmanuel Cottancin,[‡] Michel Pellarin,[‡]
Daniel Ugarte,[†] Matthias Hillenkamp,^{†,‡} Douglas S. Galvao,[†] and Varlei
Rodrigues^{*,†}

[†]*Gleb Wataghin Institute of Physics, State University of Campinas, Campinas, SP,
13083-970, Brazil*

[‡]*Institute of Light and Matter, University Lyon, Université Claude Bernard Lyon 1,
CNRS, UMR5306, Villeurbanne F-69622, France*

[¶]*These authors contributed equally to this work*

E-mail: varlei@ifi.unicamp.br

Abstract

Metal nanoparticles are omnipresent in today's applied and fundamental research. Both wet-chemical as well as physical procedures for their fabrication are well-established, where the latter is of particular interest as they supply surfactant-free particles. The particle growth has been investigated for several decades, but due to its complexity, involving kinetic and dynamic processes on various length and time scales, often only phenomenological rules of thumb are available. In this study, we report on bimetallic AgAu nanoparticles and demonstrate how the additional degree of freedom of the chemical composition can be used to derive information about how and where the particles grow, depending on two different cluster source types (hollow magnetron vs. laser vaporization). The chemical composition is quantified on the single-particle level using electron-induced x-ray spectroscopy (STEM-EDS) and shows significant differences for the two fabrication routes. Based on Molecular Dynamics and Monte-Carlo simulations, we derive that for hollow cylindrical sources both the mean particle size and the chemical composition are determined within the plasma region, where particles not only grow but also evaporate low-boiling silver. The comparably large plasma plays a decisive role here, as opposed to planar magnetron or laser vaporization sources, where no such evaporation is observed. These results shed light into the complex cluster growth and help understand and optimizing nanoscale fabrication processes.

INTRODUCTION

Metallic nanoparticles have been used in numerous applied and fundamental studies, involving different research fields, amongst others, optics,¹ catalysis,² photocatalysis,³ electronics,⁴ magnetism,⁵ spintronics^{6,7} and sensing.⁸ Two main nanoparticle fabrication approaches can be differentiated: wet chemistry and physical techniques. The latter has the advantage of providing surfactant-free nanoparticles; among them, gas-phase synthesis is the most frequently used at present.⁹ Despite a large amount of research on such metal nanoparticles,

the detailed kinetics and dynamics of the aggregation processes still need to be fully understood, and classical nucleation theory can only provide a qualitative understanding.¹⁰ One of the most used techniques since cluster science's early days is the laser vaporization source (LVS), as shown schematically in Figure 1a.¹¹ Here a laser hits the metal target rod and ignites a confined plasma of the order of a mm^3 for a very short time, typically several nanoseconds. Next, an inert gas quenches the hot plasma, and the metal vapor condenses into clusters and nanoparticles before rapidly cooling by a supersonic expansion.¹² This is a typical example of cluster fabrication by successive steps: metal vapor generation, supersaturation and condensation, and finally, termination of growth through dilution in the molecular beam.

A second popular method for nanoparticle fabrication is based on magnetron sputtering cluster sources (MSCS), which have been extensively investigated over the last years.^{10,13–23} The general interpretation of cluster formation (also by some of the authors of this article) was that metal atoms are sputtered into the gas phase in the discharge and aggregate into clusters and nanoparticles by nucleation, successive atom addition and finally cluster coalescence all along the path between the discharge and the exit orifice of the aggregation region (cf. Figure 1b). This picture was supported by the simple and reproducible observation that increasing the distance between the magnetron head, and exit orifice monotonously increases the size of produced particles. Thus the particle growth was supposed to occur along the same general lines as described above for the LVS, despite the geometric and temporal differences. The magnetron discharge forms a torus of several cm in diameter and some mm in thickness, operated in almost all cases in continuous mode (dc). When used with bimetallic targets, both types of sources, LVS and MSCS, have produced nanoparticles with the same chemical composition as the targets.^{17,24}

However, more recent works have started challenging this description for the magnetron source. The authors of^{25,26} have monitored the aggregation of Cu and Ag into nanoparticles inside the aggregation tube by in situ X-ray scattering and optical spectroscopy of the

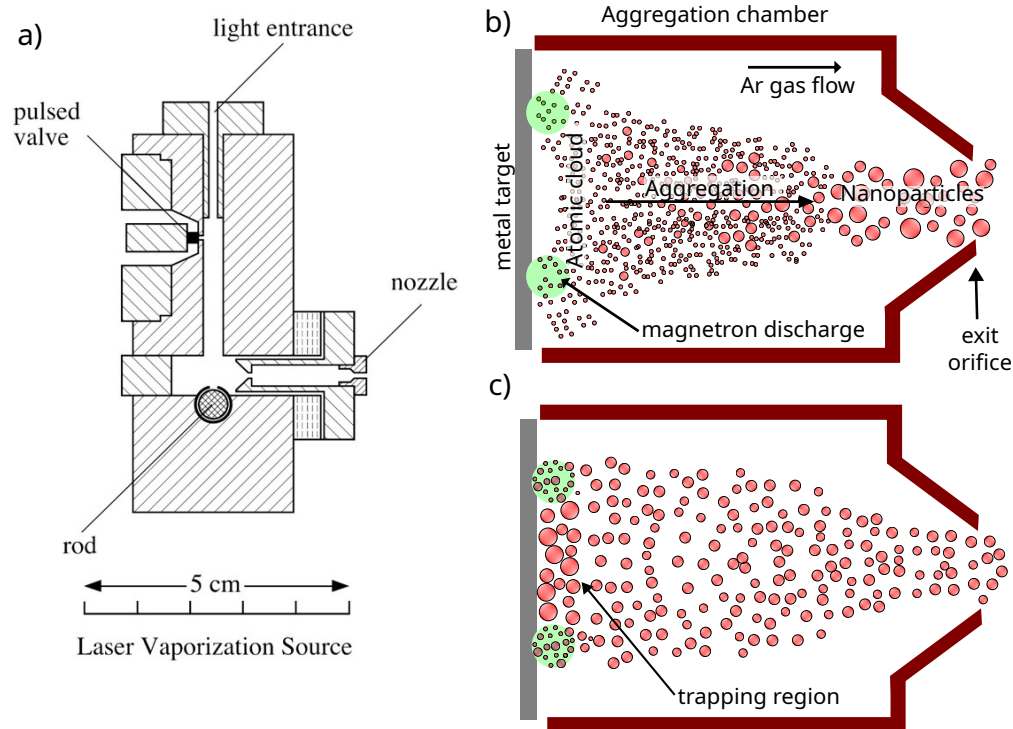


Figure 1: a) Scheme of a laser vaporization source. A laser pulse hits a rod target, eroding it and producing a localized plasma of $\sim 1 \text{ mm}^3$ for a very short time. The plasma is quenched by a pulse of inert gas that condensates the metal vapor into nanoparticles. (b-c) Schematic of a magnetron sputtering cluster source with its round metal target, usually 1 or 2 inches in diameter. The magnetron discharge forms a torus and erodes the target, producing the metal vapor that is used to form the nanoparticles. (b) The standard picture of nanoparticle formation starts from the atomic metal vapor, followed by the nucleation, successive atom addition, and finally, cluster coalescence all the way between the discharge and the exit orifice of the aggregation chamber, usually a few hundred millimeters long. (c) Recent works by Kousal et al.^{25,26} propose that the nanoparticles are formed very close to the sputter target and not all along the aggregation chamber. Also, they demonstrate that trapping regions exist in the center of the plasma torus, where the biggest nanoparticles are trapped.

silver surface plasmon resonance. They show that, contrary to the general interpretation, the nanoparticles are, in fact, formed in the very same region of the sputter target and not throughout the flow toward the end of the aggregation region. On the contrary, they demonstrated that the nanoparticles are significantly bigger in the vicinity of the discharge than after leaving the discharge area. The authors attribute this behavior to “trapping regions” in the center of the plasma torus and several centimeters above the sputter target, where inhomogeneities in the viscous flow of the inert gas lead to reduced velocities. However, the initial assumption is maintained, where particles can only grow bigger but not decrease in size inside the source. This means that if larger particles are present close to the discharge, they must be trapped or expelled from the formed beam somewhere.

In this article, we contrast these observations with experiments performed using a magnetron sputtering cluster source in the hollow cylindrical configuration (HC-MSCS),²¹ see Figure 2a-c. In the HC-MSCS, the target is a metal wire or several twisted wires of the same or different metals on the axis of a cylinder. An Argon plasma is formed inside the cylinder (anode) to erode the axial target (cathode), forming a cloud of metal used to generate the nanoparticles. In this setup, the plasma occupies a much larger volume than in the regular planar magnetron geometry (25 mm diameter and 50 mm long). Here we study bimetallic AuAg nanoparticles and exploit the additional degree of freedom of chemical composition to obtain more information about the aggregation process in our magnetron cluster source. In particular, we observe significant discrepancies between the chemical composition of the sputter target and the fabricated bimetallic nanoparticles (BNPs). This observation seems contradictory to >25 years of research using laser vaporization sources (LVS)²⁷ in one of the participating groups, where the average chemical composition of the investigated BNPs was typically determined to be very close to that of the target rod.^{24,28,29} Furthermore, also for a planar magnetron source, a chemical composition identical to that of the sputter target has been reported.¹⁷ We thus propose to exploit the obvious dependence of cluster fabrication on the exact design of the source to obtain more information about the underlying physical

processes. Our results show that for the HC-MSCS geometry, aggregation and evaporation/fragmentation processes occur in the plasma region, where collisions heat the BNPs, modifying their relative composition through evaporation.

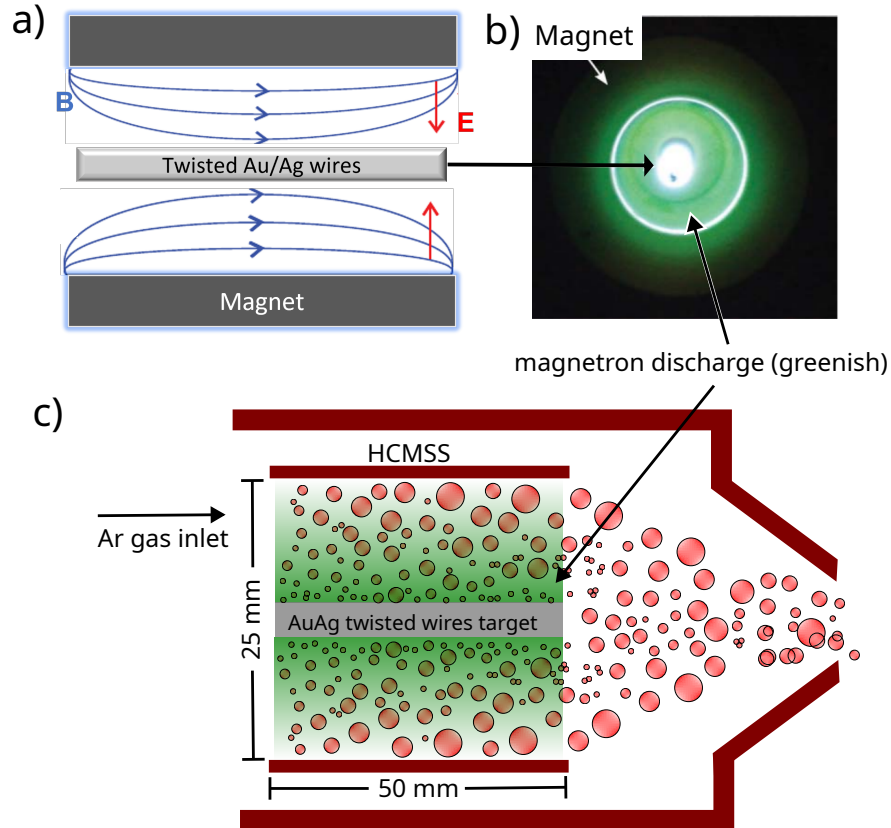


Figure 2: (a) Schematic of the hollow cylindrical magnetron sputtering (side view). The target (cathode) is in the center, and the anode corresponds to the whole cylindrical structure around it. Magnets are located in the cylindrical walls, and soft iron at the magnet extremities is used to ensure the closure of the magnetic flux lines. (b) Photo of the front view with plasma. Note the greenish color around the target, typically seen in silver plasma. (c) Schematic of the HC-MSCS mechanism of nanoparticle growth. The nanoparticles are formed in the hot plasma region (green). Large particles start growing at the beginning of the plasma region (furthest away from the exit orifice); they spend more time in the plasma than small particles formed at the end of the plasma.

METHODS

Nanoparticle Synthesis

Magnetron sputtering source:²¹ Bimetallic ($\text{Au}_x\text{Ag}_{1-x}$) NPs have been produced using a homemade gas aggregation cluster source as illustrated in Figure 1, where a cylindrical magnetron is used to sputter atoms from a central target made of twisted Au and Ag wires. A series of electrostatic lenses are used to reduce the BNP kinetic energy to achieve a “soft landing” on TEM ultrathin carbon lacey copper grid (for a ~ 4 nm in diam. NP, this corresponds to ~ 0.05 eV/atom). The NP size distribution contained in the molecular beam can be followed in situ by time-of-flight mass spectrometry (TOF-MS). TEM images indicate that the NP size distribution follows a log-normal function (mean diameter ~ 4 nm, width ~ 3 nm; see Figure S1 in Supporting Information). Three different bimetallic nanoparticle samples (A, B, C) were used in the present study whose Au content is established by a proper choice of Au:Ag twisted wires (1:1, 1:2, and 1:3, respectively). Sample D was prepared using a laser vaporization source:¹¹ A doubled Nd:YAG laser (532 nm) is focused onto the surface of an $\text{Ag}_{50}\text{Au}_{50}$ target rod, and the generated plasma is quenched in a continuous He flow. Nanoparticles form in the volume of several mm^3 above the target before being swept into a vacuum through a 1 mm nozzle, creating a supersonic expansion in which the nanoparticles are extremely and efficiently cooled. The charged fraction of the nanoparticle beam is then mass-selected in a quadrupole deviator²⁷ before being deposited fragmentation-free onto TEM grids.

Electron Microscopy: Data Acquisition and Processing

In order to measure the average chemical composition of samples A, B, and C, Energy Dispersive X-ray Spectroscopy (EDS) was performed in an ensemble of NPs, using an open parallel TEM beam with a long counting time to increase X-ray total intensity, while minimizing radiation damage (dose ~ 10 e-/ \AA^2). This measurement was performed in a JEM

2100F. The quantitative analysis of the EDS data followed the Cliff-Lorimer approach.³⁰ Despite the quantitative precision and accuracy of recovering the average composition with this method, spatially resolved information is still required to quantify the chemical composition of each individual nanoparticle. The acquisition parameters were optimized to generate reliable statistics and do not produce beam-induced modification of the sample, measuring at 80 kV to reduce knock-on damage,³¹ and composition changes.³² The probe diameter was between 0.7 - 1.0 nm, the beam current between 300-500 pA, and the dwell time between 200-400 ms, with a pixel size of 0.5 nm. The results were processed and treated using machine learning approaches to improve quantitative EDS chemical analysis, as described in our previous works.^{33,34} This measurement was performed in a JEM 2100F, and a Titan-Themis AC corrected from LNNano-Brazil. For sample D, the average chemical composition was calculated from an ensemble of 24 NPs measured individually by STEM-EDS. Here, the error is derived from standard error propagation rules. For sample D, the probe diameter was between 0.3 - 0.5 nm, beam current ~ 1 nA. NPs were measured with pixels size between 0.2 - 0.5 nm and dwell time between 50 - 200 ms, obtaining Au counts in the interval of 2,000 - 8,000 for 6 nm NPs. This measurement was performed in a JEOL NeoArm at Hubert Curien Laboratory at St. Etienne University, France. Data were processed using HyperSpy,³⁵ an open-source electron microscopy python package.

Molecular Dynamics Simulations

All MD simulations were performed with the open-source Large-scale Atomic/Molecular Massively Parallel Simulator (LAMMPS).³⁶ Ag/Au atomic interactions for all simulations were modeled by the Embedded-Atom Method (EAM), with parameters obtained from Zhou *et al.*³⁷ The dimensions of the simulation box are $L_x = L_y = L_z = 50$ nm. The initial atomic gas compositions were chosen such that the Au content is kept fixed (5000 atoms). The number of Ag atoms for each case is 45000 (10% in Au), 15000 (25% in Au), 7500 (40% in Au), and 5000 (50% in Au). The dynamics of any system simulated through MD is described

in a given ensemble that constrains some chosen thermodynamical variables. For instance, a system described by a microcanonical ensemble is simulated by an NVE dynamics, where the total number of atoms N , the simulation box volume V , and the total energy E are not modified by the integration of the equations of motion. Similarly, an NVT dynamics lead the system to a desired temperature T .

The initial gas configuration was initially thermalized using an NVE ensemble for 100 ps. Then, the gas was cooled down to $T = 300$ K during 1 ns with the addition of a Langevin thermostat and a temperature damping of $10^4 dt$ that is a hundred times larger than the minimum recommended $100 dt$ in order to assure high-quality results, where $dt = 0.1$ fs is the timestep used in all simulations in this work. After this, we let the system thermalize at the same 300 K during 2 ns, where a system with few-atom clusters was reached, and no further growth of nanometer-sized particles was observed.

We simulated the evaporative cooling of Au-Ag nanoparticles with 25%, 50%, and 75% of Au. Detail on how to build our model nanoparticles are given in the Supporting Information. First, we linearly increased the temperature of each nanoparticle from 100 K to 3000 K during 100 ps in an NVT dynamics. Then, we performed NVE molecular dynamics on the hot nanoparticles for 20 ns and observed the temperature decay as each system lost atoms, and their Ag-Au content was mapped as a function of the simulation time.

Force-Bias Monte Carlo

Force-Bias Monte Carlo (FBMC) was performed for 5×10^{11} steps at a target temperature of 300 K. FBMC runs are also implemented in LAMMPS. The cluster analysis was provided by the Open Visualization Tool (OVITO).³⁸ From the generated geometry files, we were able to obtain the number of atoms in each cluster. The nanoparticle diameters ($D = 2R$) were estimated from $R = R_W N^{1/3}$, where R_W is the Wigner radius (~ 0.16 for both Ag and Au) and N is the total number of atoms of each cluster.

RESULTS AND DISCUSSIONS

Experimental

We have studied three different BNP samples produced by the HC-MSCS: A, B, and C using three different targets: 1/1, 1/2, and 1/3 Au/Ag twisted wires, respectively (see Methods section for details). To correctly estimate an atomic cloud composition, we used the sputter yield of Au and Ag as 0.20 and 0.27 atoms/ion, respectively,³⁹ taking the plasma energy in the sputtering as 100 eV. Table 1 summarizes the estimated aggregation cloud Au/Ag content, henceforth called cloud composition. We note that Au and Ag abundance is slightly different from the initial target Au/Ag ratio due to the sputter yield correction. The uncertainty of the relative sputter yield dominates the estimated error in the atomic cloud composition.

Table 1: Au atomic fraction of the different BNP syntheses. Samples A, B, and C were prepared using the HC-MSCS, while sample D was produced using a laser vaporization BNP source. BNPs chemical composition quantification was obtained by Energy Dispersive X-ray Spectroscopy (EDS).

	Sample A	Sample B	Sample C	Sample D
Metal target	0.50 ± 0.01	0.33 ± 0.01	0.25 ± 0.01	0.50 ± 0.01
Atomic cloud	0.42 ± 0.03	0.27 ± 0.03	0.20 ± 0.03	0.50 ± 0.01
BNPs ensemble	0.727 ± 0.003	0.510 ± 0.005	0.500 ± 0.003	0.510 ± 0.002

To quantitatively evaluate the chemical composition of individual BNPs, we use the Scanning Transmission Electron Microscopy spatial resolution associated with the X-ray energy-dispersive spectroscopy (STEM-EDS). Quantitative chemical analyses were performed using the Cliff-Lorimer method and machine learning procedures^{30,33-35,40} (See Supporting Information for more details). Initially, the chemical composition was measured for an ensemble of nanoparticles using an open parallel TEM beam with a long counting time to increase the total X-ray intensity while minimizing radiation damage (dose $\sim 10 \text{ e}^-/\text{\AA}^2$). Table 1 presents the average experimental chemical composition of the BNPs. Unexpectedly, we observed very different values compared to the atomic cloud composition for the samples (A, B, C) prepared using the HC-MSCS. The composition of the three samples is always richer

in Au. The HC-MSCS thus does not produce BNP samples with a chemical composition on average equal to the composition of the atom cloud used for their synthesis.

In order to further investigate the BNP composition distribution, we have evaluated the composition of a set of individual BNPs. Figure 3a) shows as an example the STEM-EDS elemental map of five nanoparticles and Figure 3b) presents a representative EDS spectrum for an individual nanoparticle of 6 nm. The EDS data are then analyzed using machine learning procedures, described in detail in previous works.^{33,34} Figure 3c) shows the composition of 37 BNPs from sample C. In this sample, the chemical composition distribution is size-dependent, with BNPs of a diameter larger than 5 nm being narrowly dispersed around the average value. The smaller ones are relatively poor in Au compared to the average value. It can be clearly observed that the BNP composition does not reflect the cloud composition and that the composition shows some size dependence.

To compare these BNPs composition features with similar BNPs produced in a different experimental setup, we used a laser vaporization BNP source (LVS).²⁷ The BNP sample from the LVS is thereafter called sample D, and its composition information is also presented in Table 1. In sample D, the chemical composition measured for the BNPs is directly related to the cloud composition. This feature can also be seen in Figure 4, where the mean value of the dispersion in Au atomic fraction is $\sim 1\%$ close to the expected nominal composition, with a dispersion of $\sim 2\%$ in the BNP composition distribution. Additionally, no chemical composition size-dependent is observed for the measured diameter range.

Simulations

In order to elucidate the role of the different physical processes occurring in the source on the Au/Ag content of the resultant nanoparticles, we resort to molecular simulation techniques. Simulation techniques have been extensively used to study BNP's energetic stability,^{41,42} phase transitions⁴³ and core-shell segregation,⁴⁴⁻⁴⁸ as well as nanoparticle coalescence⁴⁹⁻⁵¹ and growth.⁵²⁻⁵⁴ It is important to emphasize that these studies usually consider the behavior

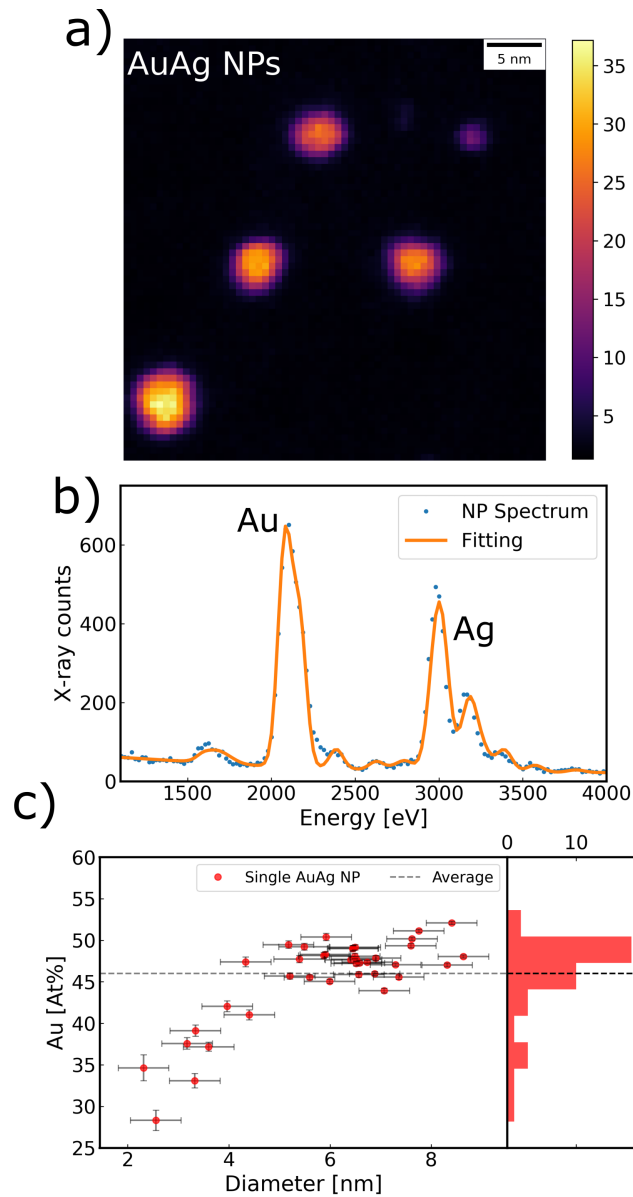


Figure 3: STEM-EDS measurement of AuAg BNPs. a) Elemental mapping obtained using the characteristic x-ray intensities from Au $M\alpha$ and Ag $L\alpha$ emission lines. b) Representative EDS spectrum for a single BNP and its fitting to integrate the peak intensity. c) Chemical composition for AuAg BNPs as a function of diameter from sample C. The red points are the composition quantification for individual BNPs, and the dashed line is the average value measured using open beam TEM-EDS. The $K_{AuAg} = 0.85 \pm 0.01$ Cliff-Lorimer constant was calibrated from a reference sample of known chemical composition. Note that all BNPs are richer in Au than the sputter target (25%).

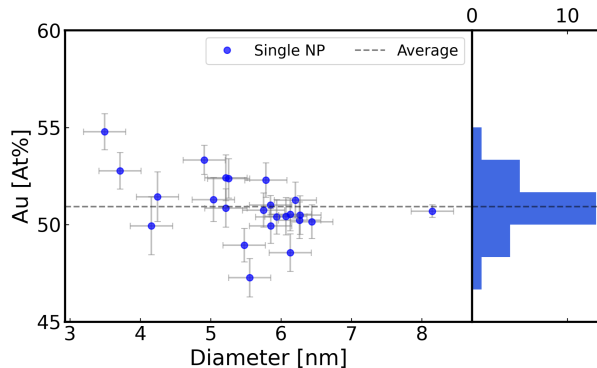


Figure 4: Chemical composition quantification of individual AuAg BNPs measured by STEM-EDS. BNPs are produced by laser vaporization source, where the BNPs are cold compared with the HC-MSCS setup. The nominal composition of the metal target (50:50) is reproduced in the measured BNPs. The $K_{AuAg} = 0.69 \pm 0.01$ Cliff-Lorimer constant was calibrated from a reference sample of known chemical composition.

of a single nanoparticle at the end of their simulations. In order to get correspondence between the composition of atomic gas and the average composition of an ensemble of BNPs, we need an approach that allows the analysis of many NP growth processes in a way that the statistical behavior can be inferred.

In this work, we simulated two distinct situations describing (i) BNP growth and aggregation from an atomic cloud with a given Au/Ag composition and; (ii) the evaporation of a single BNP initially at a high temperature. By simulating the first case, we can confirm that BNPs produced solely by atom (or cluster) aggregation possess average compositions consistent with the Au/Ag content of the initial atomic cloud. In this way, a different process must explain the unexpected average compositions of BNPs produced by HC-MSCS. Next, we simulated the second situation, where we have a hot BNP that loses atoms due to its elevated temperature (escape/evaporation). For the latter case, we considered only a single BNP to avoid unnecessary complexities and analyzed the changes in composition resulting only from high temperatures.

The first simulation case, henceforth referred to as BNP growth, was performed by considering a system composed of N_g (N_s) atoms of gold (silver) randomly distributed inside a cubic simulation box, as shown in Figure 5 (a). The relative amount of gold and silver was

such that we have Au compositions of 10%, 25%, 40%, and 50% (for more details, see the Methods section). We used Molecular Dynamics (MD) to initially simulate a hot gas of gold and silver atoms at a temperature of $T = 2000$ K. Then, the gas was quenched to $T = 300$ K, where the system loses energy very rapidly and forms a set of small atomic clusters (Figure 5 (b)). After this, we let the system thermalize at the same 300 K for a long time, and the system still consisted of small clusters made of a few atoms. The timescale of nanometer-sized particle growth is computer-demanding by molecular dynamics simulations because there must be many low-energy collisions where atoms are incorporated in larger clusters and, subsequently, in a larger nanoparticle. In other words, the growth of BNPs from small atomic clusters are rare events that MD simulations cannot reproduce unless the simulations run for a long time. In fact, some previous works⁵⁵⁻⁵⁷ have applied MD for complete BNPs growth but for simulations time on the order of tens of ns for a set of Au/Ag BNPs, and for a single BNP for simulation time as long as $1.5 \mu\text{s}$. One way to overcome these limitations and accelerate the growth process is to use Force-Bias Monte Carlo (FBMC) to aggregate small clusters into nanoparticles. In our case, we first started with an atomic gas randomly distributed in the simulation cell and ran an MD simulation for a predetermined number of steps to obtain small atomic aggregates. These clusters will work as seeds for the further growth of larger nanoparticles through using the FBMC for another predetermined number of steps. In Monte Carlo techniques, the use of random numbers to update the state of the system can overcome large energy barriers imposed by physical paths to reach equilibrium, as in the case of simulated growth using MD simulations. Therefore, we adopted a sequential scheme of MD/FBMC to generate bimetallic nanoparticles with tens (or a few hundred) atoms. This hybrid approach that uses MD and FBMC to simulate a process that has two stages on different time scales has already been employed in previous works.⁵⁸⁻⁶⁰ Also, this same scheme was used to study core-shell segregation trends in BNPs.⁶¹ To our knowledge, there are no works in literature that use these two techniques combined to accelerate the growth of many BNPs in a single simulation. Examples of the resulting BNPs grown by an

FBMC run are shown in Figure 5 (c), where we computed each individual nanoparticle’s Au/Ag composition using cluster analysis. All detailed information and simulation parameters are given in the Methods section. The composition of each individual BNP is shown as a point in Figure 5 (d), where dashed horizontal lines represent the average compositions. It can be seen that the average BNP composition is close to the initial gas composition. Nominal values and standard deviations for these quantities are reported in the caption of Figure 5. These results indicate that the discrepancy in the final nanoparticle compositions in the experiments arises from a different reason rather than just the chemical composition of the sputtered atoms from the target alone. The larger number of points for smaller Au percentages occurs because they have a larger number of atoms in the initial gas (explained in the Methods section) and, thus, can form more nanoparticles at the end of the simulation.

To describe high-temperature effects on Au/Ag BNPs, we considered a reasonably large nanoparticle of 4000 atoms (diameter of ~ 5.0 nm) with three different Au compositions (25%, 50%, and 75%). Then, we carried out MD runs in an NVE (or microcanonical) ensemble and monitored the temperature change of the BNP as time evolved. For more details regarding the types of ensembles used in MD simulations, see the Supporting Information. We observe that atoms escape from the BNP due to its high temperature. Since the microcanonical ensemble describes an isolated system inside the simulation box, where the energy is (on average) conserved, any temperature changes of the BNP are solely due to the evaporation of atoms. This process is known as evaporative cooling. For the evaporative cooling simulations, we need a BNP hot enough such that atoms can escape from the BNP due to the high temperature. On the other hand, we could not start from the temperature where the evaporation of the BNP would take place abruptly. With this in mind, the choice of the initial temperature should be intermediate between the melting point of silver and that of gold in such a nanoscale environment to stimulate the escape of atoms at the beginning of the simulation followed by a decreased rate of evaporation as the time evolves. In order to have a range of initial temperatures, we performed a thermal ramp from 100 K to 5000 K on

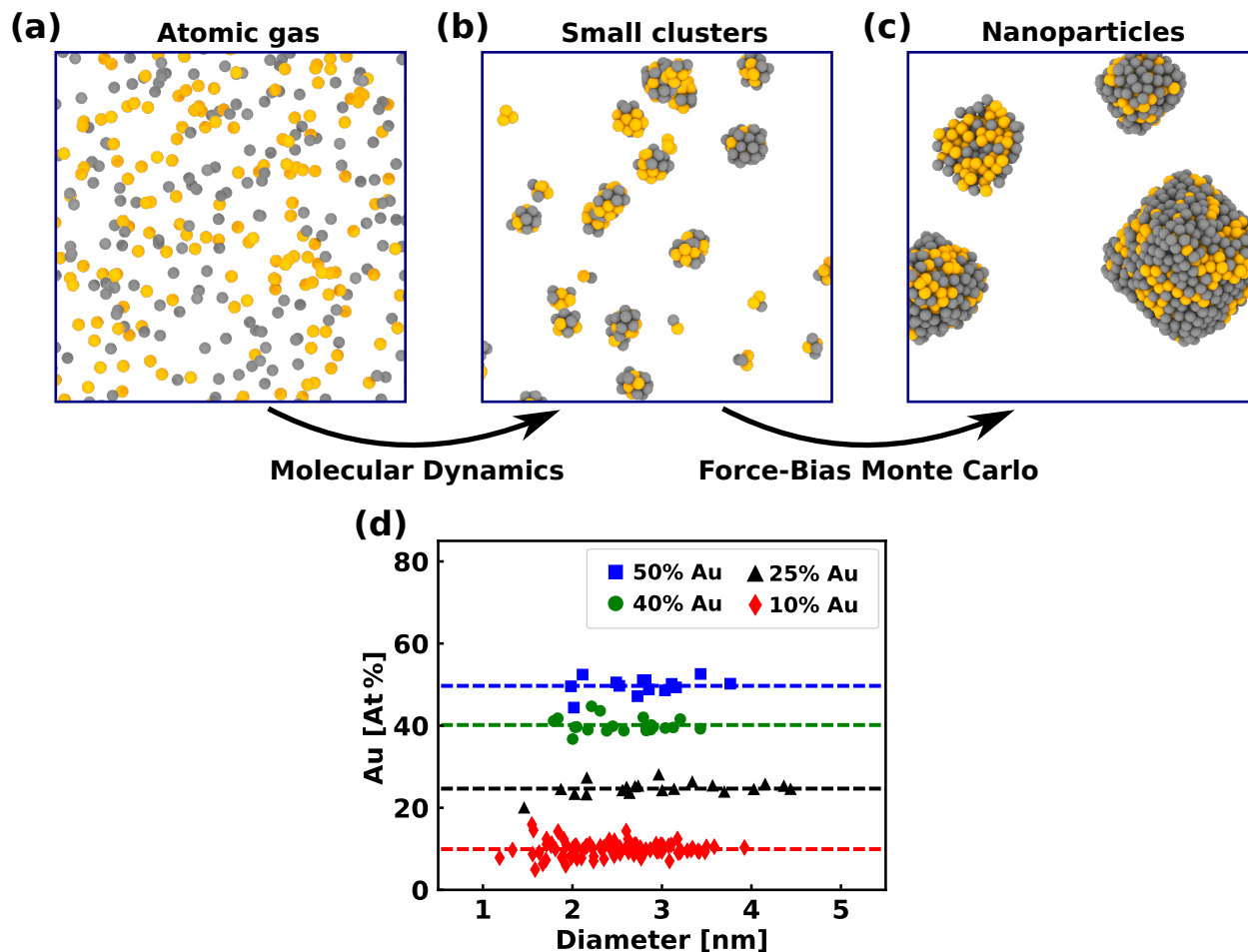


Figure 5: Hybrid MD/FBMC approach to study Au-Ag nanoparticle aggregation. (a) An initial atomic Au/Ag gas evolves to (b) a set of small clusters using MD. Then, FBMC is implemented to mimic a longer-timescale process of (c) nanometer-sized particle growth. For the sake of simplicity, in (a)-(c), we just show a piece of the whole simulation box. The chemical composition of individual nanoparticles is given by points with shapes indicated by the legend. The average composition (with their corresponding standard deviation) of each are $50 \pm 2\%$ (for 50% in Au), $40 \pm 2\%$ (for 40% in Au), $25 \pm 2\%$ (for 25% in Au) and $10 \pm 2\%$ (for 10% in Au).

the BNPs of each composition. We monitored the instantaneous atomic composition of each BNP until it completely evaporated. This gives us an insight into the range of temperatures where the BNPs start to evaporate. Thus, by observing the composition as a function of the temperature from the ramp simulations (see Figure S2 for more details), we observed that in the range between $\sim 2500 - 3500$ K we have silver atoms starting to escape the BNP, indicating that the evaporation of silver in this system lies in this temperature range. We then decided to choose 3000 K as the initial temperature. The melting temperature of nano-sized metallic particles can be difficult to choose as it can be determined by either energy or self-diffusion coefficient,⁶² and, thus, we chose the evaporation point as the initial temperature. The chosen nanoparticle size was such that it is in the range of size-independent composition, as shown in Figure 3 (c). Initially, the nanoparticle starts to lose atoms due to its elevated temperature. This leads to a temperature decrease as a consequence of losing atoms with higher kinetic energies (cooling by evaporation), as can be seen in Figure 6 (a). Such decay is similar to the temperature evolution observed in water droplets under evaporative cooling.⁶³ This Au-rich nanoparticle slower decay rate is expected since gold has a higher melting point than silver, which helps to stabilize nanoparticles with a larger gold content.^{64,65} It is important to emphasize that the nanoscale behavior of metals is very distinct from that of bulk where, for instance, the evaporation points of nanoscale metals are considerably lower than that of their bulk counterparts.^{64,66}

As the time evolves in the evaporative cooling simulations, only Ag atoms escape from the nanoparticle (independently of its chemical composition), as shown in Figure 6 (b). Similar to the reasons explained above for the greater stability of Au-rich nanoparticles, the weaker metallic bonding of silver contributes to this significant difference in evaporation rates between the two elements. This indicates that the higher Au compositions of the nanoparticles reported in Table 1 are a consequence of the evaporation of silver atoms from each nanoparticle before the sample holder deposition.

The role of core-shell segregation in the evaporation process is important to account for

surface effects on the selective evaporation of Ag. Figure 6 (c) illustrates the core and shell definitions used in this work. We analyzed the core and shell composition as a function of the simulation time, shown in Figure 6 (d). We can see that Au content increases in the core and decreases in the shell. Since none of the gold atoms evaporated during the time span in our simulations, we can infer that there is a migration of gold from shell to core as it has a higher surface energy and, more importantly, a higher bulk cohesive energy, which was recently found to be of fundamental importance in determining core-shell segregation trends in bimetallic nanoparticles.⁶¹ Both core and shell Ag moieties decrease with time, showing that even silver atoms in the core migrate to the surface, where they escape (are ejected) from the nanoparticle. This higher tendency of Ag evaporation is dominant, and it holds even for Au-rich nanoparticles

Discussion

Our simulations describe the two main processes in forming BNPs in cluster sources and allow us to estimate their importance in the two cases discussed here. Firstly, nucleation and coalescence, on the one hand, lead to particle growth and heating due to released binding energy. They are the most important at comparably low temperatures, where supersaturation and slow evaporation kinetics favor the sticking of atoms. Secondly, at higher temperatures, on the other hand, close to or above the size-dependent evaporation temperature of the nanoparticle material, atoms are evaporated, and the particle size decreases, i.e., while coalescence increases the particle temperature, evaporative cooling decreases it.

In the case of a hollow cylindrical magnetron source, the observed deviations in the chemical composition somehow represent a counterintuitive situation. Typically, nanoparticle growth only depends on the atomic vapor density and composition, in which the latter reflects the grown BNP average composition. Only the presence of a high-temperature environment changes the relative composition through evaporation. This evaporation process happens simultaneously with nucleation inside the HC-MSCS. Thus, we cannot conceptually

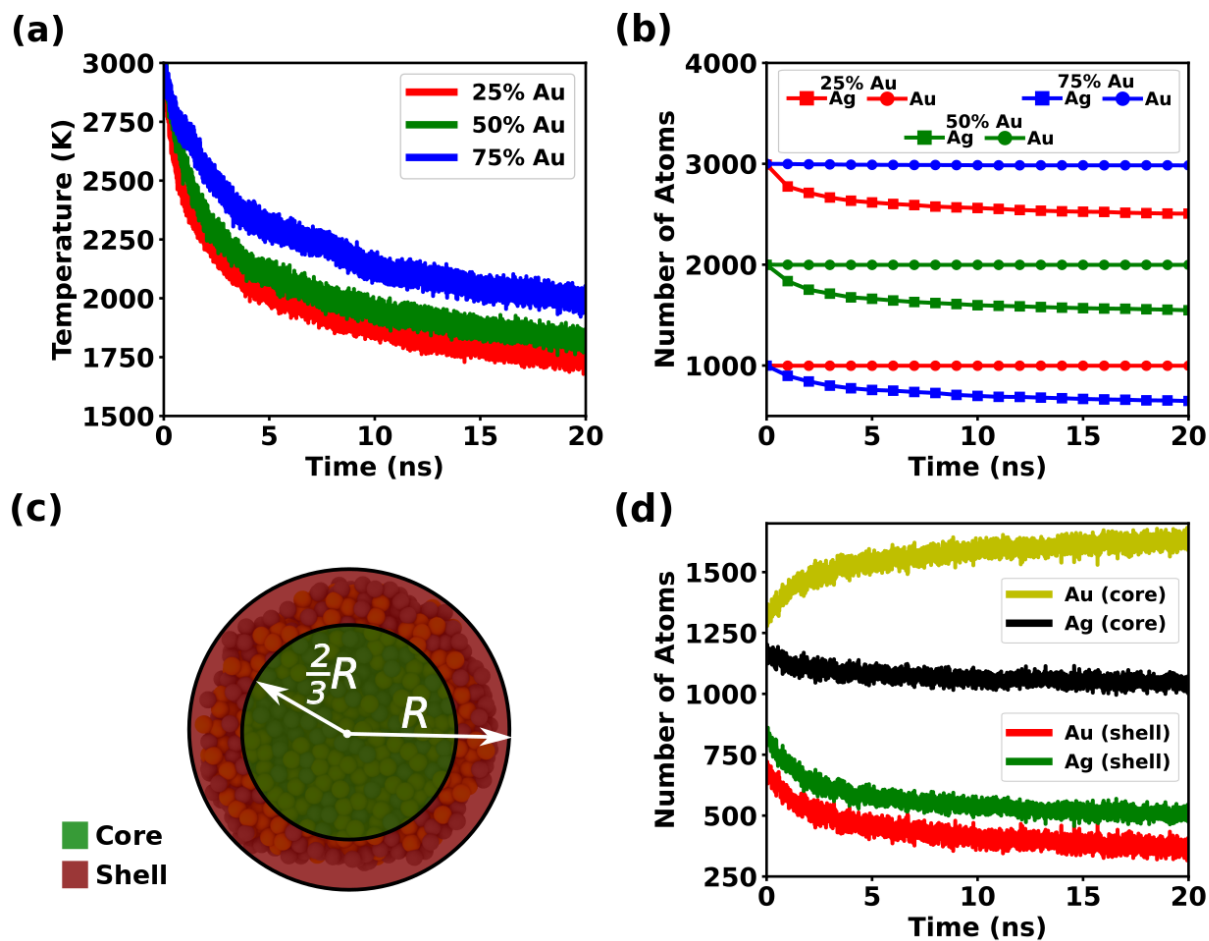


Figure 6: Evaporative cooling simulations for nanoparticles with 25%, 50%, and 75% in Au. (a) Time evolution of temperature decay as a consequence of atoms that escape from the nanoparticle initially at 3000 K. (b) The number of atoms of Au and Ag as a function of time, where squares denote silver and circles denote gold content. The same color refers to simulations of a given chemical composition. (c) Definition of core and shell, where the core is a $2R/3$ -radius sphere concentric with the nanoparticle and the $R/3$ -thickness spherical shell is the outside region representing the shell. (d) Core-shell resolved Au-Ag composition of a 50% gold nanoparticle, where the colors are indicated in the legend.

separate high-temperature BNP's evaporation and simultaneous lower-temperature condensation.

Our simulation results and the observed deviations in the BNPs' chemical composition indicate that, in the HC-MSCS, all condensation and evaporation processes occur in the plasma region, where collisions with accelerated ions heat the BNPs. Even though the plasma removes atoms from the target by ion collisions and not thermally (so-called cold plasma), high temperatures in the metal vapor are achievable. Furthermore, the BNPs are heated by the binding energy of added atoms during aggregation. We find a stable kinetic state only in the region close to the target, where the particle temperature and residence time are defined by the various source parameters, such as gas flow conditions and discharge power, among others. We cannot obtain information about the exact temperature inside the plasma, and it might, at some point, be even higher than the evaporation temperature of gold, leading to increased evaporation of both metals from possibly present large particles. However, the important point is that, eventually, the particles reach a temperature between the two evaporation points, the crucial regime in which the chemical composition can be modified. After leaving the plasma region, the nanoparticle temperature decreases through collisions with the carrier gas, and it rapidly cools below the evaporation temperature, and evaporative cooling and composition variation stop. This effect is enhanced because the melting temperature increases with increasing particle size.

The interpretation of the nanoparticle growth process proposed above is supported by the size dependence on the chemical composition. The smallest BNPs stay only a short time in the growth region, i.e., they start growing near the end of the plasma region, here, the end of the cylinder within which the plasma is confined, cf. figure 2c). They are, thus, less heated and lose fewer silver atoms, with the smallest generated clusters being close to the target composition.

These considerations lead us to redefine the concept of particle growth in magnetron sources. Contrary to the widespread acceptance, atomic addition throughout the trajectory

towards the exit orifice seems negligible. The cluster size is largely defined in the plasma region close to the sputtering target, as already observed by Kousal et al.^{25,26} The fact that an increase in the distance between the magnetron head and the exit of the aggregation chamber increases the particle size must then be linked to other parameters. Notably, the gas flow conditions affect both the residence time within the plasma and the transport through the aggregation tube.²⁶ The interpretation of cluster growth occurring exclusively in the plasma region is confirmed by the observation that metal redeposition principally takes place within the plasma tube and only to a very small extent onto the walls of the condensation tube.

However, we must remark that the exact geometry of the source, especially the plasma, is of fundamental importance in this discussion. While planar magnetron sources generate cluster beams without apparent electronic shell closures or odd-even oscillations,¹⁵ they are observed in the cylindrical setup discussed here,²¹ similarly to sources based on high-energy sputtering in vacuum.⁶⁷ This observation indicates that the generated clusters are eventually hotter in the cylindrical setup than in the planar one, reflecting the differences in time the atoms spent inside the plasma. Furthermore, in laser vaporization sources, the growth mechanisms must also be in a cold environment, as reflected by the chemical composition of the BNPs. We interpret nucleation and coalescence as the determining mechanism; evaporative cooling does not seem to play a significant role. This is a reasonable assumption considering that the laser pulses are only of the order of 5 ns and the plasma is thus rapidly quenched to temperatures well below the boiling temperatures of the metals, contrary to magnetrons, where the dc plasma continuously heats the vapor and the clusters throughout their fabrication. Two more mechanisms for nanoparticle heating must also be discussed. First, in magnetron cluster sources, some plasma often opens between the cathode and the aggregation tube, forming a large "afterburner" leading to significantly increased ionization yields. In our cylindrical setup experiments, we have made sure to confine the plasma between the cathode and anode, thereby minimizing potential heating throughout the aggregation tube. Second, suppose the cluster ions are accelerated between the aggregation tube exit and the

following ion optics (a skimmer). In that case, the collisions in this high-pressure region can easily lead to cluster heating and fragmentation, as evidenced by the appearance of odd-even oscillations in the cluster abundance. For the experiments discussed here, we have kept the potential difference between the tube and skimmer small enough to avoid significant acceleration-induced heating.

Finally, we would like to comment on three other possible explanations for the chemical composition deviation in our AuAg BNPs. First, we can consider that silver and gold could be sputtered at different solid angles, as has been observed before for pulsed laser desorption under high vacuum conditions.⁶⁸ However, in our case, the viscous carrier gas flow inside the hollow magnetron mixes up all the plasma components (gas, metal atoms, and nanoparticles) and sweeps them toward the plasma exit. A second possible explanation could be a preferential sputtering of gold vs. silver, leading to gold-enriched BNPs. We can rule out this, as Ag's sputter yield is higher than Au's. Furthermore, this should lead to the enrichment of one metal over the other in the target rod. BNPs fabricated at the beginning and end of the target lifetime, however, showed no significant difference in chemical compositions. Lastly, different diffusion rates for Ag and Au in the gas flow between the plasma region and the aperture of the condensation tube could also lead to changes in the chemical composition if the lighter silver atoms migrate more quickly towards the aggregation tube walls and out of the beam. We, however, believe this effect to be minor, if at all present. In the hollow magnetron geometry, the vast majority of metal that does not condensate into clusters is redeposited onto the walls of the anode, i.e., inside the plasma region. This observation can be seen as another indication of the cluster growth happening solely within the plasma. But even in the more open planar magnetron geometry, no such increased diffusion has been seen, as evidenced by the averaged chemical composition of AgAu BNPs.¹⁷

On the basis of these considerations, we can now relate our results to the recent literature. In,^{25,26} the authors suggest that large nanoparticles are generated in the plasma region of their magnetron source but cannot leave the source due to hydrodynamic trapping. We

propose that a second mechanism should be considered, which is the evaporative cooling described above. Additional to hydrodynamical trapping, the authors may have measured a steady state large diameter population inside the plasma, which rapidly decreases in size in the outer region of the plasma, where the particles are still heated but no longer grow.

CONCLUSIONS

Although the study of metallic nanoparticles in the gas phase is an area with decades of development, the detailed knowledge of the nanoparticle growth process still presents fundamental questions. There are several routes for the formation of nanoparticles, from the way the metal cloud is generated to the strategy for its aggregation. However, all these processes are always quite complex, and it is challenging to infer the different phenomena that occur there directly. Our chemical composition analysis of gas aggregated BNPs using a hollow cylindrical magnetron sputter source cannot be understood in the framework of classical nucleation theory⁶⁹ or even considering more recent descriptions^{25,26} of the planar magnetron geometry. In our case, the composition differs from that of the sputter target, which is impossible to rationalize simply in terms of the Au/Ag fraction in the initial atomic gas generated by sputtering, as shown by atomistic simulations of an MD/FBMC hybrid approach. On the contrary, evaporative cooling simulations using MD show that the selective evaporation of silver is responsible for the Au enrichment in BNPs synthesized by HC-MSCSs. Thus, we can conclude that the nanoparticle growth must occur in a high-temperature region, where the plasma heats the newly formed BNPs. Further experiments are planned to verify our interpretation, e.g., using AuCu as BNP material. These two metals have similar evaporation temperatures, so we expect much less deviation between the target and BNP chemical composition.

Our results shed new light on the knowledge of the process of nanoparticle formation in the gas phase. Although our results are not directly transferable to sources with other

geometries and smaller plasma regions, they demonstrate that atom evaporation can play an important role. Notable in planar magnetrons, it might, in some cases, help to understand size variations within the source,²⁵ whereas in other cases, nucleation takes place at lower temperatures, and large out-of-equilibrium structures are frozen.⁷⁰ This study furthermore indicates that, in the HC-MSCS, NPs undergo annealing during their formation, which influences the structural characteristic of the particles, producing crystalline and compact ground-state atomic arrangements (see example in Figure S3). This fact could be exploited for the in-flight fabrication of relaxed structures. Conversely, larger clusters obtained by LVS have been shown to be ramified, depending on the metal melting temperature.⁷¹

We can furthermore continue, based on these conclusions, with quantitative structural analyses using a Pair Distribution Function derived from electron diffraction.⁷² Also, our interpretation can be verified by studying the CoPt system, which has been demonstrated to display chemical order upon annealing.²⁴ In addition, we have gained a deeper understanding of how to model and control the parameters of hollow cylindrical magnetron sources to prepare high-quality model samples with chemical composition control, opening up new possibilities for studies and applications in essential areas such as catalysis, for example.

Acknowledgement

This work was supported by the Brazilian Agencies Fundação de Amparo à Pesquisa do Estado de São Paulo (Fapesp proc. 2007/01722-9, 2014/01045-0 and 2019/09882-2), Conselho Nacional de Desenvolvimento Científico e Tecnológico (CNPq proc. 555647/2006-4, 577046/2008-0, 402571/2016-9, 306513/2017-0, 162541/2018-0 and 402676/2021-1) and Fundo de Apoio ao Ensino, à Pesquisa e Extensão, Universidade Estadual de Campinas (Faepex 2395/22). Access to the FEG-TEM/STEM from the Brazilian Nanotechnology National Laboratory is acknowledged (LNNANO, grant No. ME-22329, TEM-23436, TEM-24286, TEM-C1 - 26046, TEM-C1-25091). This work was also supported by the the French

Campus France Eiffel Excellency Scholarship Program (EIFFEL-DOCTORAT 2020/P760767) and the French National Research Agency (ANR) via the project ‘SchNAPSS’, ANR- 21-CE09-0021. Some of the samples were elaborated at the PLYRA@iLMtech facility with technical support from O. Boisron, C. Albin, C. Clavier and S. Hermelin. The authors also thank Stephanie Reynaud for technical support at the Consortium Lyon Saint-Etienne de Microscopie (CLYM).

Supporting Information Available

Histogram of AuAg NPs diameter distribution measured by TEM; Thermal evaporation of an Au-Ag nanoparticle, structural and chemical composition evolution of the nanoalloy as a function of the number of atoms and initial compositions; HAADF STEM image of AuAg BNPs produced by the HCMSS.

References

- (1) Campos, A.; Troc, N.; Cottancin, E.; Pellarin, M.; Weissker, H.-C.; Lermé, J.; Kociak, M.; Hillenkamp, M. Plasmonic Quantum Size Effects in Silver Nanoparticles are Dominated by Interfaces and Local Environments. *Nat. Phys.* **2019**, *15*, 275–280.
- (2) Heiz, U., Landman, U. E., Eds. *Nanocatalysis*; Springer, 2007.
- (3) Aslam, U.; Rao, V. G.; Chavez, S.; Linic, S. Catalytic conversion of solar to chemical energy on plasmonic metal nanostructures. *Nature Catalysis* **2018**, *1*, 656.
- (4) Mirigliano, M.; Milani, P. Electrical conduction in nanogranular cluster-assembled metallic films. *Adv. Phys. X* **2021**, *6*, 1908847.
- (5) Oyarzún, S.; Tamion, A.; Tournus, F.; Dupuis, V.; Hillenkamp, M. Size effects in the

- magnetic anisotropy of embedded cobalt nanoparticles: from shape to surface. *Sci. Rep.* **2015**, *5*, 14749.
- (6) Serrano-Guisan, S.; Di Domenicantonio, G.; Abid, M.; Abid, J.-P.; Hillenkamp, M.; Gravier, L.; Ansermet, J.-P.; Félix, C. Enhanced magnetic field sensitivity of spin-dependent transport in cluster-assembled metallic nanostructures. *Nat. Mater.* **2006**, *5*, 730.
- (7) Hai, P. N.; Ohya, S.; Tanaka, M. Long spin-relaxation time in a single metal nanoparticle. *Nat. Nanotechnol.* **2010**, *5*, 593–596.
- (8) Hensel, R. C.; Braunger, M. L.; Oliveira, B.; Shimizu, F. M.; Oliveira, O. N.; Hillenkamp, M.; Riul, A.; Rodrigues, V. Controlled Incorporation of Silver Nanoparticles into Layer-by-Layer Polymer Films for Reusable Electronic Tongues. *ACS Appl. Nano Mater.* **2021**, *4*, 14231.
- (9) Huttel, Y., Ed. *Gas-Phase Synthesis of Nanoparticles*; WILEY-VCH Verlag, 2017.
- (10) Haberland, H. *Gas-Phase Synthesis of Nanoparticles*; John Wiley & Sons, Ltd, 2017; Chapter 1, pp 1–21.
- (11) Perez, A.; Melinon, P.; Dupuis, V.; Bardotti, L.; Masenelli, B.; Tournus, F.; Prevel, B.; Tuaille-Combes, J.; Bernstein, E.; Tamion, A. et al. Functional nanostructures from clusters. *Int. J. Nanotechnol.* **2010**, *7*, 523–574.
- (12) De Toro, J. A.; Normile, P. S.; Binns, C. *Gas-Phase Synthesis of Nanoparticles*; John Wiley & Sons, Ltd, 2017; Chapter 3, pp 39–55.
- (13) Haberland, H.; Mall, M.; Moseler, M.; Qiang, Y.; Reiners, T.; Thurner, Y. Filling of micron-sized contact holes with copper by energetic cluster impact. *J. Vac. Sci. Technol. A* **1994**, *12*, 2925–2930.

- (14) Palmer, R. E.; Pratontep, S.; Boyen, H. G. Nanostructured surfaces from size-selected clusters. *Nat. Mater.* **2003**, *2*, 443–448.
- (15) Hillenkamp, M.; Di Domenicantonio, G.; Félix, C. Monodispersed metal clusters in solid matrices: A new experimental setup. *Rev. Sci. Instrum.* **2006**, *77*, 025104.
- (16) Smirnov, B. M.; Shyjumon, I.; Hippler, R. Flow of nanosize cluster-containing plasma in a magnetron discharge. *Phys. Rev. E* **2007**, *75*, 066402.
- (17) Belić, D.; Chantry, R. L.; Li, Z. Y.; Brown, S. A. Ag-Au nanoclusters: Structure and phase segregation. *Appl. Phys. Lett.* **2011**, *99*, 171914.
- (18) Hartmann, H.; Popok, V. N.; Barke, I.; von Oeynhausen, V.; Meiwes-Broer, K.-H. Design and capabilities of an experimental setup based on magnetron sputtering for formation and deposition of size-selected metal clusters on ultra-clean surfaces. *Rev. Sci. Instrum.* **2012**, *83*, 073304.
- (19) Zhang, C.; Tsunoyama, H.; Akatsuka, H.; Sekiya, H.; Nagase, T.; Nakajima, A. Advanced Nanocluster Ion Source Based on High-Power Impulse Magnetron Sputtering and Time-Resolved Measurements of Nanocluster Formation. *J. Phys. Chem. A* **2013**, *117*, 10211–10217.
- (20) Pilch, I.; Söderström, D.; Brenning, N.; Helmersson, U. Size-controlled growth of nanoparticles in a highly ionized pulsed plasma. *Appl. Phys. Lett.* **2013**, *102*, 033108.
- (21) de Sá, A. D. T.; Oiko, V. T. A.; di Domenicantonio, G.; Rodrigues, V. New experimental setup for metallic clusters production based on hollow cylindrical magnetron sputtering. *J. Vac. Sci. Technol. B* **2014**, *32*, 061804.
- (22) Khojasteh, M.; Kresin, V. V. Influence of source parameters on the growth of metal nanoparticles by sputter-gas-aggregation. *Appl. Nanosci.* **2017**, *7*, 875–883.

- (23) Sanzone, G.; Yin, J.; Sun, H. Scaling up of cluster beam deposition technology for catalysis application. *Front. Chem. Sci. Eng.* **2021**, *15*, 1360–1379.
- (24) Tournus, F.; Blanc, N.; Tamion, A.; Hillenkamp, M.; Dupuis, V. Dispersion of magnetic anisotropy in size-selected CoPt clusters. *Phys. Rev. B* **2010**, *81*, 220405.
- (25) Kousal, J.; Shelemin, A.; Schwartzkopf, M.; Polonskyi, O.; Hanus, J.; Solar, P.; Vaidulych, M.; Nikitin, D.; Pleskunov, P.; Krtous, Z. et al. Magnetron-sputtered copper nanoparticles: lost in gas aggregation and found by in situ X-ray scattering. *Nanoscale* **2018**, *10*, 18275.
- (26) Drewes, J.; Ali-Ogly, S.; Strunskus, T.; Polonskyi, O.; Biederman, H.; Faupel, F.; Vahl, A. Impact of argon flow and pressure on the trapping behavior of nanoparticles inside a gas aggregation source. *Plasma Process. Polym.* **2022**, *19*, 2100125.
- (27) Alayan, R.; Arnaud, L.; Bourgey, A.; Broyer, M.; Cottancin, E.; Huntzinger, J. R.; Lermé, J.; Vialle, J. L.; Pellarin, M.; Guiraud, G. Application of a static quadrupole deviator to the deposition of size-selected cluster ions from a laser vaporization source. *Rev. Sci. Instrum.* **2004**, *75*, 2461.
- (28) Rousset, J. L.; Cadrot, A. M.; Cadete Santos Aires, F. J.; Renouprez, A.; Mélinon, P.; Perez, A.; Pellarin, M.; Vialle, J. L.; Broyer, M. Study of bimetallic Pd–Pt clusters in both free and supported phases. *J. Chem. Phys.* **1995**, *102*, 8574.
- (29) Dupuis, V.; Robert, A.; Hillion, A.; Khadra, G.; Blanc, N.; Roy, D. L.; Tournus, F.; Albin, C.; Boisron, O.; Tamion, A. Cubic chemically ordered FeRh and FeCo nanomagnets prepared by mass-selected low-energy cluster-beam deposition: a comparative study. *Beilstein J. Nanotechnol.* **2016**, *7*, 1850.
- (30) Cliff, G.; Lorimer, G. W. The quantitative analysis of thin specimens. *Journal of Microscopy* **1975**, *103*, 203–207.

- (31) Egerton, R. F. Choice of operating voltage for a transmission electron microscope. *Ultramicroscopy* **2014**, *145*, 85–93.
- (32) Braidy, N.; Jakubek, Z. J.; Simard, B.; Botton, G. A. Quantitative energy dispersive X-ray microanalysis of electron beam-sensitive alloyed nanoparticles. *Microscopy and microanalysis* **2008**, *14*, 166–175.
- (33) Moreira, M.; Hillenkamp, M.; Divitini, G.; Tizei, L. H. G.; Ducati, C.; Cotta, M. A.; Rodrigues, V.; Ugarte, D. Improving quantitative EDS chemical analysis of alloy nanoparticles by PCA denoising: part I, reducing reconstruction bias. *Microscopy and microanalysis* **2022**, 1–12.
- (34) Moreira, M.; Hillenkamp, M.; Divitini, G.; Tizei, L. H. G.; Ducati, C.; Cotta, M. A.; Rodrigues, V.; Ugarte, D. Improving quantitative EDS chemical analysis of alloy nanoparticles by PCA denoising: part II. uncertainty intervals. *Microscopy and microanalysis* **2022**, 1–9.
- (35) De La Peña, F.; Ostasevicius, T.; Fauske, V. T.; Burdet, P.; Jokubauskas, P.; Nord, M.; Sarahan, M.; Prestat, E.; Johnstone, D. N.; Taillon, J. et al. Electron Microscopy (Big and Small) Data Analysis With the Open Source Software Package HyperSpy. *Microscopy and Microanalysis* **2017**, *23*, 214–215.
- (36) Plimpton, S. Fast Parallel Algorithms for Short-Range Molecular Dynamics. *Journal of Computational Physics* **1995**, *117*, 1–19.
- (37) Zhou, X. W.; Johnson, R. A.; Wadley, H. N. G. Misfit-energy-increasing dislocations in vapor-deposited CoFe/NiFe multilayers. *Physical Review B* **2004**, *69*, 144113.
- (38) Stukowski, A. Visualization and analysis of atomistic simulation data with OVITO—the Open Visualization Tool. *Modelling and Simulation in Materials Science and Engineering* **2010**, *18*, 015012.

- (39) Laegreid, N.; Wehner, G. K. Sputtering Yields of Metals for Ar⁺ and Ne⁺ Ions with Energies from 50 to 600 eV. *Journal of applied physics* **1961**, *32*, 365–369.
- (40) Carter, C. B., Williams, D. B., Eds. *Transmission Electron Microscopy*; Springer International Publishing: Cham, 2016.
- (41) Chen, F.; Johnston, R. L. Energetic, electronic, and thermal effects on structural properties of Ag-Au nanoalloys. *ACS Nano* **2008**, *2*, 165–175.
- (42) Liao, T.-W.; Yadav, A.; Hu, K.-J.; van der Tol, J.; Cosentino, S.; D’Acapito, F.; Palmer, R. E.; Lenardi, C.; Ferrando, R.; Grandjean, D. et al. Unravelling the nucleation mechanism of bimetallic nanoparticles with composition-tunable core-shell arrangement. *Nanoscale* **2018**, *10*, 6684–6694.
- (43) Qi, W. H.; Lee, S. T. Phase stability, melting, and alloy formation of Au-Ag bimetallic nanoparticles. *The Journal of Physical Chemistry C* **2010**, *114*, 9580–9587.
- (44) Curley, B. C.; Rossi, G.; Ferrando, R.; Johnston, R. L. Theoretical study of structure and segregation in 38-atom Ag-Au nanoalloys. *The European Physical Journal D* **2007**, *43*, 53–56.
- (45) Calvo, F.; Cottancin, E.; Broyer, M. Segregation, core alloying, and shape transitions in bimetallic nanoclusters: Monte Carlo simulations. *Physical Review B* **2008**, *77*, 121406.
- (46) Cerbelaud, M.; Ferrando, R.; Barcaro, G.; Fortunelli, A. Optimization of chemical ordering in AgAu nanoalloys. *Physical Chemistry Chemical Physics* **2011**, *13*, 10232–10240.
- (47) Deng, L.; Hu, W.; Deng, H.; Xiao, S.; Tang, J. Au–Ag Bimetallic Nanoparticles: Surface Segregation and Atomic-Scale Structure. *The Journal of Physical Chemistry C* **2011**, *115*, 11355–11363.

- (48) Li, L.; Li, X.; Duan, Z.; Meyer, R. J.; Carr, R.; Raman, S.; Koziol, L.; Henkelman, G. Adaptive kinetic Monte Carlo simulations of surface segregation in PdAu nanoparticles. *Nanoscale* **2019**, *11*, 10524–10535.
- (49) Faccin, G. M.; San-Miguel, M. A.; Andres, J.; Longo, E.; da Silva, E. Z. Computational modeling for the ag nanoparticle coalescence process: A case of surface plasmon resonance. *The Journal of Physical Chemistry C* **2017**, *121*, 7030–7036.
- (50) Abbaspour, M.; Akbarzadeh, H.; Salemi, S.; Lotfi, S. Investigation of possible formation of au@m (M = cu, ir, pt, and rh) core-shell nanoclusters in a condensation-coalescence process using molecular dynamics simulations. *Industrial & engineering chemistry research* **2018**, *57*, 14837–14845.
- (51) Grammatikopoulos, P.; Sowwan, M.; Kioseoglou, J. Computational modeling of nanoparticle coalescence. *Advanced Theory and Simulations* **2019**, 1900013.
- (52) Harjunmaa, A.; Nordlund, K. Molecular dynamics simulations of Si/Ge cluster condensation. *Computational Materials Science* **2009**, *47*, 456–459.
- (53) Turner, C. H.; Lei, Y.; Bao, Y. Modeling the atomistic growth behavior of gold nanoparticles in solution. *Nanoscale* **2016**, *8*, 9354–9365.
- (54) Punjani, K.; Bhimalapuram, P. Study of shape changes during nanoparticle growth using Kinetic Monte Carlo simulation: a case study on gold nanoparticles. *Journal of Chemical Sciences* **2021**, *133*, 101.
- (55) Akbarzadeh, H.; Shamkhali, A. N.; Mehrjouei, E. Ag-Au bimetallic nanoclusters formed from a homogeneous gas phase: a new thermodynamic expression confirmed by molecular dynamics simulation. *Physical Chemistry Chemical Physics* **2017**, *19*, 3763–3769.
- (56) Vernieres, J.; Steinhauer, S.; Zhao, J.; Chapelle, A.; Menini, P.; Dufour, N.; Diaz, R. E.; Nordlund, K.; Djurabekova, F.; Grammatikopoulos, P. et al. Gas Phase Synthe-

- sis of Multifunctional Fe-Based Nanocubes. *Advanced functional materials* **2017**, *27*, 1605328.
- (57) Grammatikopoulos, P. Atomistic modeling of the nucleation and growth of pure and hybrid nanoparticles by cluster beam deposition. *Current opinion in chemical engineering* **2019**, *23*, 164–173.
- (58) Rao, M.; Berne, B. J. On the force bias Monte Carlo simulation of simple liquids. *The Journal of Chemical Physics* **1979**, *71*, 129–132.
- (59) Mees, M. J.; Pourtois, G.; Neyts, E. C.; Thijsse, B. J.; Stesmans, A. Uniform-acceptance force-bias Monte Carlo method with time scale to study solid-state diffusion. *Physical Review B* **2012**, *85*, 134301.
- (60) Neyts, E. C.; Bogaerts, A. Combining molecular dynamics with Monte Carlo simulations: implementations and applications. *Theoretical chemistry accounts* **2013**, *132*, 1320.
- (61) Eom, N.; Messing, M. E.; Johansson, J.; Deppert, K. General Trends in Core-Shell Preferences for Bimetallic Nanoparticles. *ACS Nano* **2021**, *15*, 8883–8895.
- (62) Ercolessi, F.; Andreoni, W.; Tosatti, E. Melting of small gold particles: Mechanism and size effects. *Physical Review Letters* **1991**, *66*, 911–914.
- (63) Schlesinger, D.; Sellberg, J. A.; Nilsson, A.; Pettersson, L. G. M. Evaporative cooling of microscopic water droplets in vacuo: Molecular dynamics simulations and kinetic gas theory. *The Journal of Chemical Physics* **2016**, *144*, 124502.
- (64) Guisbiers, G.; Mendoza-Cruz, R.; Bazán-Díaz, L.; Velázquez-Salazar, J. J.; Mendoza-Perez, R.; Robledo-Torres, J. A.; Rodriguez-Lopez, J.-L.; Montejano-Carrizales, J. M.; Whetten, R. L.; José-Yacamán, M. Electrum, the Gold-Silver Alloy, from the Bulk Scale

- to the Nanoscale: Synthesis, Properties, and Segregation Rules. *ACS Nano* **2016**, *10*, 188–198.
- (65) Okamoto, H.; Massalski, T. B. The Ag-Au (Silver-Gold) system. *Bulletin of Alloy Phase Diagrams* **1983**, *4*, 30–38.
- (66) Lasserus, M.; Schnedlitz, M.; Knez, D.; Messner, R.; Schiffmann, A.; Lackner, F.; Hauser, A. W.; Hofer, F.; Ernst, W. E. Thermally induced alloying processes in a bimetallic system at the nanoscale: AgAu sub-5 nm core-shell particles studied at atomic resolution. *Nanoscale* **2018**, *10*, 2017–2024.
- (67) Conus, F.; Lau, J. T.; Rodrigues, V.; Félix, C. High sensitivity absorption measurement of small metal clusters embedded in an argon matrix. *Rev. Sci. Instrum.* **2006**, *77*, 113103.
- (68) Urbassek, H.; Sibold, D. Gas-phase segregation effects in pulsed laser desorption from binary targets. *Phys. Rev. Lett.* **1993**, *70*, 1886.
- (69) Mélinon, P. *Gas-Phase Synthesis of Nanoparticles*; John Wiley & Sons, Ltd, 2017; Chapter 2, pp 23–38.
- (70) Xia, Y.; Nelli, D.; Ferrando, R.; Yuan, J.; Li, Z. Y. Shape control of size-selected naked platinum nanocrystals. *Nat. Commun.* **2021**, *12*, 3019.
- (71) Alayan, R.; Arnaud, L.; Broyer, M.; Cottancin, E.; Lermé, J.; Vialle, J. L.; Pellarin, M. Morphology and growth of metal clusters in the gas phase: A transition from spherical to ramified structures. *Phys. Rev. B* **2006**, *73*, 125444.
- (72) Corrêa, L. M.; Moreira, M.; Rodrigues, V.; Ugarte, D. Quantitative Structural Analysis of AuAg Nanoparticles Using a Pair Distribution Function Based on Precession Electron Diffraction: Implications for Catalysis. *ACS Applied Nano Materials* **2021**, *4*, 12541–12551.

TOC Graphic

